

Quantitative Principles for Precise Engineering of Sensitivity in Graphene Electrochemical Sensors

Ting Wu, Abdullah Alharbi, Roozbeh Kiani, and Davood Shahrjerdi*

A major difficulty in implementing carbon-based electrode arrays with high device-packing density is to ensure homogeneous and high sensitivities across the array. Overcoming this obstacle requires quantitative microscopic models that can accurately predict electrode sensitivity from its material structure. Such models are currently lacking. Here, it is shown that the sensitivity of graphene electrodes to dopamine and serotonin neurochemicals in fast-scan cyclic voltammetry measurements is strongly linked to point defects, whereas it is unaffected by line defects. Using the physics of point defects in graphene, a microscopic model is introduced that explains how point defects determine sensitivity. The predictions of this model match the empirical observation that sensitivity linearly increases with the density of point defects. This model is used to guide the nanoengineering of graphene structures for optimum sensitivity. This approach achieves reproducible fabrication of miniaturized sensors with extraordinarily higher sensitivity than conventional materials. These results lay the foundation for new integrated electrochemical sensor arrays based on nanoengineered graphene.

The ease of fabrication and operation of carbon-based electrochemical sensors gives them the potential to enable a new class of integrated sensor systems with wide-ranging applications from drug development to clinical diagnostics. To support these applications, the sensor system requires high spatial density (i.e., a dense packing of miniaturized sensors) and consistent operations across the sensor array (i.e., sensors with accurate

and homogeneous sensitivity). Moreover, high-precision applications require electrodes with high sensitivity. Although the availability of advanced fabrication techniques would allow miniaturization of carbon-based electrochemical sensors,^[1–4] satisfying the low variability and high accuracy requirements of sensitivity across a dense sensor array remains a difficult challenge.

The sensitivity of this family of sensors is tied to the structural properties of the electrode material.^[5–7] It is natural for the material to have atomic-level structural inhomogeneity, which can cause variability in the electrode sensitivity among sensors. Due to the random spatial distribution of the structural inhomogeneities in the electrode material, this variability becomes more pronounced with reducing sensor size. To account for the variability and also to determine the electrode sensitivity, the

common practice is to calibrate each sensor through postmanufacturing measurements, which involves creating “calibration curves” by measuring the sensor response to known concentrations of analytes.^[8] Although this strategy is applicable for dealing with individual devices or a small sensor array, it is highly inefficient for the implementation of large-scale integrated sensor systems. A more tractable approach is to produce carbon-based sensors with precise sensitivity by engineering the material synthesis. However, the efficacy of this approach hinges on a quantitative understanding of the precise relationship between the structural properties of the material at the nanoscale and the sensitivity of the electrode at a macroscale.


Pioneering studies, including those by McCreery and coworkers,^[9–12] have suggested that the electron transfer in sp^2 -based carbon electrodes (e.g., carbon nanotube and graphene-related materials) is enhanced at the edge plane sites. Others have inferred that oxygen-containing functional groups in these materials can also promote electron transfer.^[13,14] Since electron transfer is a fundamental process that determines sensitivity, step edges and oxygen-containing functional groups are commonly assumed to be responsible for the experimental observations of enhanced sensitivity in sensors made from sp^2 carbon materials.^[15–18] In recent years, however, researchers have pointed to additional active electrochemical sites in sp^2 carbon materials by using scanning electrochemical cell microscopy (SECCM). For example, seminal studies by Unwin and coworkers^[19–23] and others^[24,25] have shown that the basal planes of sp^2 carbon materials are electrochemically active.

T. Wu, A. Alharbi, Prof. D. Shahrjerdi
Electrical and Computer Engineering
New York University
Brooklyn, NY 11201, USA
E-mail: davood@nyu.edu

Prof. R. Kiani
Center for Neural Science
New York University
New York, NY 10003, USA

Prof. R. Kiani
Neuroscience Institute
New York University Langone Medical Center
New York, NY 10016, USA

Prof. D. Shahrjerdi
Center for Quantum Phenomena
Physics Department
New York University
New York, NY 10003, USA

 The ORCID identification number(s) for the author(s) of this article can be found under <https://doi.org/10.1002/adma.201805752>.

DOI: 10.1002/adma.201805752

Moreover, it has been suggested that point defects are active electrochemical sites in monolayer graphene.^[26] Further, using an improved SECCM, Güell et al. have shown the enhanced electrochemical activity of step edges in graphene.^[27] While the literature on electron transfer is still evolving,^[28–30] these past studies have advanced our knowledge about the correlation between nanoscale structural properties and electron transfer in sp^2 -based carbon electrodes.

However, there still remain significant gaps in our knowledge pertaining to how different structural properties of sp^2 carbon materials quantitatively determine the sensitivity of an electrode. These knowledge gaps exist because an electrode material, which is a macroscopic system, often simultaneously contains a variety of nanoscale features (defects or functional groups) in its structure, which past research has identified as active electrochemical sites. Consequently, two questions critical to precise engineering of a sensor remain unanswered: Which of those nanoscale features in the material structure affect the electrode sensitivity the most? And, more importantly, how must one tune their quantity to precisely achieve a desired sensitivity? Given that the electronic band structure is altered by introducing defects or functional groups in a material structure, the answer to the latter question requires accurate microscopic models that can quantitatively predict sensitivity from the changes in the electronic band structure. Such predictive models are severely lacking, yet are critical for developing a sensor device technology, where one can reliably produce miniaturized sensors with the desired characteristics of high and homogeneous sensitivities across an array.

Our study here focuses on providing a predictive model for graphene sensors. The model depicts, on a microscopic level, how the sensitivity of graphene and its electronic band structure are affected by structural defects in graphene. We achieve this model by systematically studying the sensitivity of miniaturized electrochemical sensors made of disordered multilayer graphene to neurochemicals (dopamine and serotonin) using fast-scan cyclic voltammetry (FSCV) technique. Graphene is an excellent test vehicle for this study since, as we show below, it is easy to produce defect-engineered graphene films with precise amounts of defects and quantify the defects using experimentally established Raman-based models.^[31–35] Specifically, we used multilayer graphene to suppress any interference from charged impurities at the interface of the graphene sensors and the oxide substrate. In fact, a recent SECCM study has shown significant variations of electron transfer across the surface of a monolayer graphene on a SiO_2 substrate.^[27] In contrast, they have also shown that the presence of multiple layers can effectively shield the electrode surface (where the electron transfer occurs) from charge impurities in the substrate. Our tight control over the sensor fabrication process, together with the accuracy and reproducibility of our material characterizations and sensor measurements, has allowed us, for the first time, to experimentally determine the accurate relationship between the average density of point defects and the FSCV sensitivity of multilayer graphene electrochemical sensors to neurochemical molecules. Importantly, uncovering this relationship allows us to propose a microscopic model that can quantitatively explain the sensitivity of multilayer graphene sensors based on the density of electronic states in the material.

We use the predictions of our microscopic model for nano-engineering the structural properties of multilayer graphene electrodes on an atomic level to precisely match a desired sensitivity. We show that our engineered electrodes exhibit up to 20 times higher sensitivity to dopamine than conventional carbon fiber (CF) electrodes in FSCV measurements.^[36–38] Moreover, we demonstrate that our model consistently applies to multilayer graphene sensors produced through different synthesis methods, promising wide applicability of our paradigm for prediction and engineering of the sensitivity of carbon-based electrochemical sensors.

To evaluate the link between the atomic structure of multilayer graphene and the sensitivity of electrodes made of it, we performed electrochemical sensing of biochemical molecules using FSCV. Owing to its good ionic specificity and subsecond detection ability, FSCV with carbon-based electrodes has been used extensively for measuring biochemical molecules in chemically complex environments such as the brain.^[15,36,39,40] We initially constructed FSCV electrodes using multilayer graphene grown by chemical vapor deposition (CVD) and measured their sensitivity to neurochemical molecules in vitro. CVD graphene films typically have different amounts of sp^2 -hybridized defects, due to minor differences in the production method, apparatus, or even the granular structure of the growth substrate.^[41,42] To increase the diversity of different defect densities in our sensor electrodes, we obtained several batches of CVD multilayer graphene films grown on nickel foils.

To fabricate electrodes, we transferred the CVD multilayer graphene films with an average thickness of 35 nm onto SiO_2/Si substrates using standard chemical layer-transfer processes.^[43–45] Using nanofabrication, we then made miniaturized sensor electrodes with a planar geometry, shown schematically in **Figure 1a**. The details of the fabrication process are given in Section S1 of the Supporting Information. We used a similar process for fabricating all devices discussed in this paper. We designed the fabrication process around two key factors. The first one is to avoid creating unintentional defects in multilayer graphene during the sensor fabrication (see Figure S3 in the Supporting Information). This consideration is particularly important when making electrodes from defect-engineered multilayer graphene, discussed later. To do so, during the fabrication process, we protected the sensing region of the electrode with a thin metal layer (Cr/Au: 5 nm/50 nm). Second, for analyzing the sensor response in our study, we used the area-normalized sensitivity. We defined the sensing region of the electrodes accurately using an SU8 encapsulating layer. This layer also protected the metal contact from exposure to the electrolyte solution. To perform the sensing experiments, we removed the protective metal stack and mounted a fluidic chamber on the samples. Figure 1b shows the top-view scanning electron microscopy (SEM) image of an example sensor array. For comparison, we also fabricated electrodes from conventional CFs (Figure S4, Supporting Information), commonly used in FSCV measurements of neurochemicals in the brain.^[37,46]

We characterized the sensitivity of the fabricated sensors through FSCV measurements of dopamine—an important neuromodulator for action-selection and reward-motivated behavior.^[47–49] During the FSCV measurement (see Section S3 in the Supporting Information for details), dopamine (the

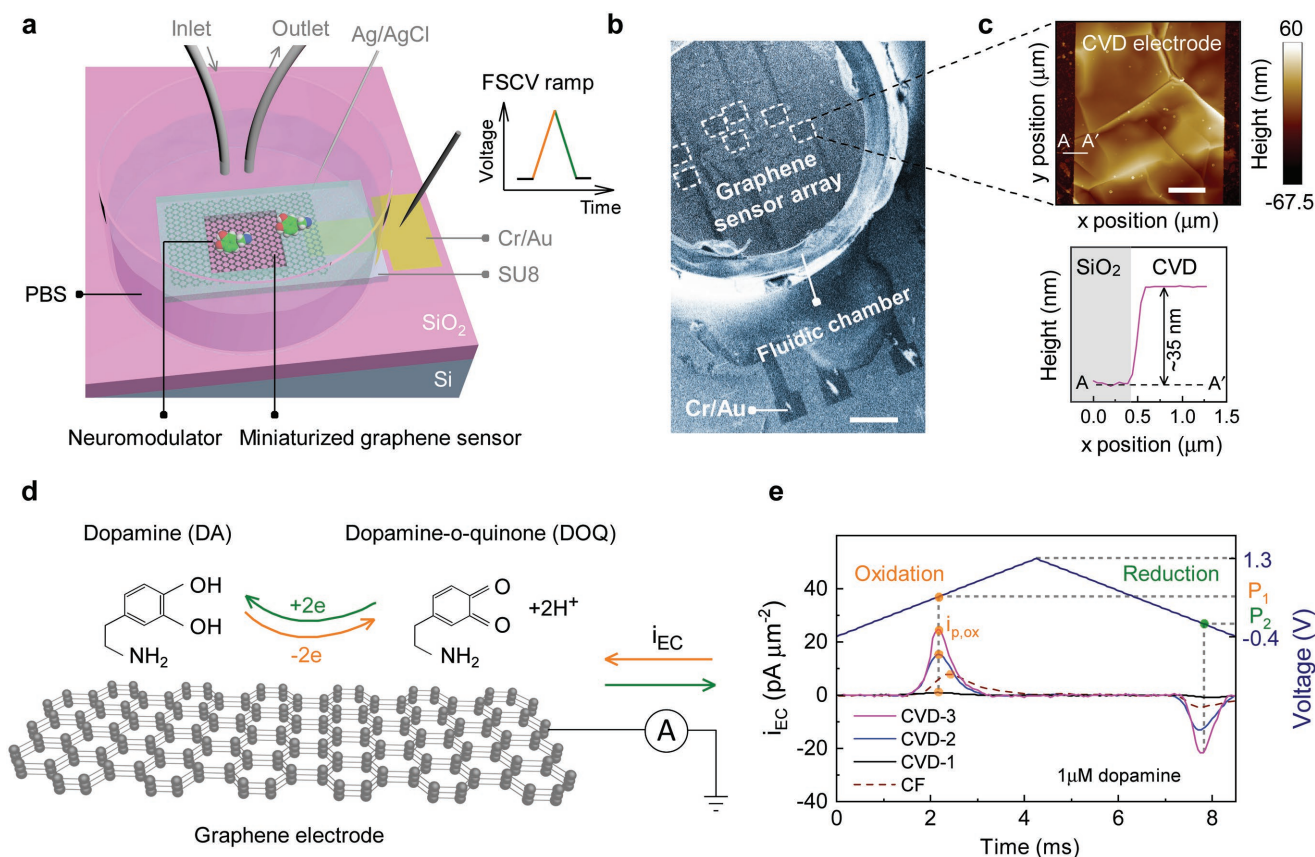


Figure 1. FSCV sensors made of multilayer graphene films with different amounts of structural defects. a) Schematics of a multilayer graphene electrode used for FSCV measurements. The multilayer graphene electrode was mounted on a SiO₂/Si substrate and connected to a Cr/Au contact. A fluidic chamber filled with PBS solution of target biochemicals (dopamine or serotonin neuromodulators) was made around the sensor. To maintain neuromodulator concentration at a desired level, fresh solution was brought to the chamber by an inlet and old solution was taken out by an outlet. b) The SEM image shows an example of our miniaturized multilayer graphene sensor array and fluidic chamber around the sensors. We used nanofabrication to build miniaturized sensors from our candidate multilayer graphene films. Scale bar is 300 μm. c) Topographic image of an example CVD multilayer graphene sensor and its thickness measured by atomic force microscopy. Scale bar is 5 μm. d) In FSCV measurements of dopamine, the voltage is applied to the sensor electrode; it first quickly ramps up, which oxidizes dopamine to dopamine-o-quinone, and then ramps down, which reduces it back to dopamine. The resulting current is measured. e) Area-normalized electrochemical current (*i*_{EC}) as a function of time in one FSCV cycle for four sample electrodes made of CVD multilayer graphene films and carbon fibers. We also show the voltage waveform applied to the electrode. In all FSCV measurements, we used a voltage scan rate of 400 V s⁻¹ and a repetition frequency of 10 Hz. P₁ and P₂ denote the oxidation and reduction peak potentials. The noticeable variations of *i*_{EC} for these sensors in response to the same dopamine concentration highlight the critical role of structural defects on sensitivity.

reductant, R) undergoes a redox reaction (Figure 1d), where it is oxidized to dopamine-o-quinone (DOQ) (the oxidant, O) by a voltage ramp-up applied to the electrode (see Figure 1a). The amplitude of the resulting oxidation current is a measure of the dopamine concentration. The voltage subsequently ramps down, causing the DOQ molecules to be reduced back to dopamine, which gives rise to a reduction current. FSCV estimates dopamine concentration based on the magnitude of the oxidation current. Electrode sensitivity represents the change in the peak of the oxidation current (*i*_{p,ox}) per unit concentration of a biomolecule (Figure S6c,d, Supporting Information). We defined unit concentration as micromolar and the area-normalized sensitivity, *S*_A, as *i*_{p,ox} at 1 × 10⁻⁶ M divided by electrode area. Because the amplitude of the electrochemical current is proportional to the geometric surface area of the sensors, normalization of sensitivity by sensor area enables comparison of sensors with diverse sizes. Surface roughness increases the

geometric surface area and can potentially bias the area-normalized sensitivity. Therefore, we estimated the total surface area of our multilayer graphene sensors by performing atomic force microscopy (AFM) and measuring surface roughness before the FSCV experiments (Figure 1c; Figures S7 and S8, Supporting Information). As a result, our area-normalized sensitivity is independent of the sensor geometry and reflects the inherent sensing property of the electrode material.

Figure 1e shows the area-normalized electrochemical current (*i*_{EC}) curves for four example electrodes (three CVD and one CF) in response to a 1 × 10⁻⁶ M dopamine solution. The orange circles on the curves denote *i*_{p,ox}. This plot and the FSCV measurements of the other CVD electrodes (Figure S9, Supporting Information) demonstrate the substantial variations in electrode sensitivity. Many sensors were minimally responsive to dopamine molecules and a few showed noticeably higher *S*_A than the CF devices. We hypothesized that the diversity

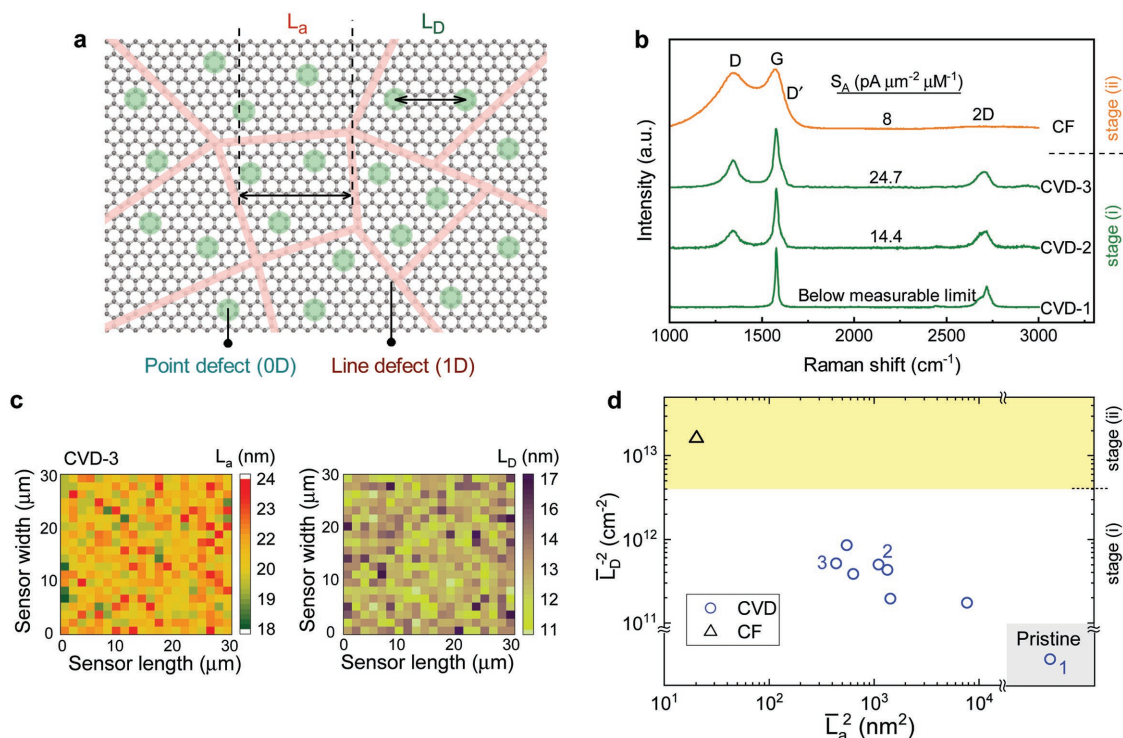


Figure 2. Quantifying structural defects in graphene electrodes. a) Line and point defects are typically present at the same time in synthetic multilayer graphene films and can be characterized by the average crystallite size, L_a , and average distance between point defects, L_D , respectively. b) To evaluate the structural properties of the CVD films, we used Raman spectroscopy. The increase of the D peak intensity for samples from bottom to top indicates the higher density of sp^2 -hybridized defects. The gradual changes of the Raman peaks also highlight the transition from a graphitic structure in stage (i) into a fully disordered sp^2 carbon in stage (ii). Conventional CFs are typically in stage (ii) as shown by the example electrode in the top row. Area-normalized sensitivity, S_A , is indicated for each sample electrode. c) Spatially resolved L_a and L_D across the sensor surface for an example CVD electrode. To estimate the average density of point and line defects, we obtained similar spatial maps for all electrodes studied in this work. d) The scatter plot of the average crystallite area (\bar{L}_a^2) and the average point defect density (\bar{L}_D^{-2}) shows that our candidate materials covered a broad range of defect densities. Numbers next to the CVD samples indicate example electrodes in (b). The yellow shading represents stage (ii) of the amorphization trajectory, while the gray box marks the detection limit of Raman for estimating the point and line defect density.

of structural defects of the sensing material was crucial for explaining the wide range of observed electrode sensitivities.

The ability to distinguish different types of defects and quantify their amounts in the electrode material is critical for revealing the connection between structural defects and the electrode sensitivity. While the types of structural defects are diverse, one simple way to classify them is based on their dimensionality. For example, defects in materials with a 2D lattice, such as graphene, are either 0D (point defects) or 1D (line defects). Examples of point defects in graphene are vacancies,^[50–52] topological defects such as Stone–Wales defect,^[51,52] and dopants.^[53] On the other hand, crystallite edges^[32] and extended dislocations^[51] are examples of line defects. Point and line defects are often simultaneously present in synthetic graphene-based materials, as shown schematically in **Figure 2a**. Physics-based models that use Raman spectroscopy data have been experimentally established for identifying and quantifying sp^2 -hybridized defects in graphene based on their dimensionality.^[31–35] Specifically, scanning tunneling microscopy (STM) measurements, which are the gold standard for determining the structure and distribution of defects on an atomic scale, are used to calibrate and validate these Raman-based quantitative models.

Figure 2b shows representative Raman spectra for a few CVD samples and a CF electrode. The distinct peaks in the Raman

spectrum of multilayer graphene films are well studied.^[54,55] The G peak appears at about 1579 cm^{-1} and signifies the sp^2 hybridization of carbon atoms. The D peak arises from the breathing modes of aromatic carbon rings and signifies sp^2 -hybridized defects. The 2D peak is the second order of the D peak, which is present only in fully sp^2 -bonded carbon materials. Changes of these peaks in Figure 2b (from bottom to top) illustrate the gradual transition of the film structure i) from a highly ordered multilayer graphene to a disordered nanocrystalline graphite and ii) finally to a fully disordered sp^2 carbon material. In stage (i), the D peak intensity increases monotonically and the 2D peak is visible in the Raman spectra. Upon transition into stage (ii), the 2D peak becomes noticeably broad and its intensity weakens dramatically. The combination of our CVD and CF electrodes covered the whole spectrum of the graphene amorphization trajectory.

We applied a theoretical method by Cançado et al.^[35] for extracting the amounts of point and line defects from the measured Raman spectra of our sensor samples. This method has also been validated using previously published STM data, illustrating its ability to unambiguously distinguish point and line defects in graphene-based samples.^[35] Although, unlike STM, the Raman-based methods lack single defect resolution, they are suitable for accurate quantification of average defect

densities in graphene films when the defect density is moderately high (i.e., $>10^{11} \text{ cm}^{-2}$). This theoretical method relies on numerical simulations based on the area ratio of the D and G peaks and the line width of the G band to derive the average crystallite size (L_a) and the average distance between point defects (L_D) within the spot size of the Raman laser. The details of our L_a and L_D calculations are given in Section S4 of the Supporting Information. We note that this methodology for quantifying defects is independent of the production method of multilayer graphene, making it suitable for our study involving CVD, graphitized (GR), and CF materials.

Since the location of defects on a sensor electrode is random, we estimated the density of each defect type on a sensor electrode by measuring the number of defects averaged over the sensor surface area. To do so, we first obtained the spatial Raman maps of our sensor electrodes and quantified L_a and L_D at each Raman spot. Figure 2c shows the spatially resolved distributions of L_a and L_D for an example CVD electrode (Figures S14–S18 in the Supporting Information show the spatial distribution of defects for all electrodes used in this study). The mean values from the L_a and L_D distributions were then used for estimating the average density of point defects ($n_{0D} = \bar{L}_D^{-2}$) and average crystallite area (\bar{L}_a^2) in our sensor samples. This methodology allows us to analyze the relationship between the area-normalized sensitivity and the density of each defect type in our carbon-based electrodes.

Figure 2d shows the scatter of \bar{L}_D^{-2} and \bar{L}_a^2 for our CVD sensor samples, highlighting the large diversity of line and point defects in our candidate sensor samples. In this plot, the gray box (in the lower right corner) marks the region, where Raman lacks accuracy for estimating point and line defect densities, because the expected L_D and L_a values are beyond the upper detection limits of Raman. The Raman spectra of samples that fall in this region typically do not show a visible D peak. We refer to those samples, with no detectable defect density by Raman, as pristine. Moreover, past Raman studies of defective graphene suggest that the onset of stage (ii) of the amorphization trajectory occurs at L_D of $\approx 4\text{--}5 \text{ nm}$.^[34] Notably, this length scale is comparable to the localization length of

the disorder-induced Raman D band at 300 K.^[56] The yellow shading in Figure 2d marks stage (ii), which includes the CF sample. In contrast, our CVD sensor samples were in stage (i) of the amorphization trajectory.

To reveal the quantitative effect of defects on the sensitivity of multilayer graphene sensors in stage (i) of the amorphization trajectory, we made a contour plot of the area-normalized sensitivity (S_A) as a function of the average crystallite area (\bar{L}_a^2) and the average point defect density (\bar{L}_D^{-2}), shown in Figure 3a. The plot shows that electrodes with similar density of point defects exhibited nearly similar S_A , regardless of their \bar{L}_a^2 . Further, S_A was amplified by increasing the density of point defects. The apparent increase of S_A with point defect density is reminiscent of a previous study reporting that point defects enhance electron transfer in irradiated monolayer graphene.^[26]

Next, we analyzed the relationship between S_A and the average point defect density (i.e., $n_{0D} = \bar{L}_D^{-2}$). Interestingly, we observed a linear relation between the area-normalized sensitivity and the point defect density when the sensing material was in stage (i), as shown in Figure 3b. The linear fit to the data in this plot is given by

$$S_A = (6.46 \pm 0.16) \times 10^{-11} (n_{0D} - n_{0D}^*) \quad (1)$$

where n_{0D}^* is the x -intercept of the linear fit and has a value of $(1.6 \pm 0.24) \times 10^{11} \text{ cm}^{-2}$. Further, S_A and n_{0D} have units of $\text{pA } \mu\text{m}^{-2} \mu\text{M}^{-1}$ and cm^{-2} , respectively. In this equation, in addition to the coefficient estimates (slope and intercept), we also provide their standard errors. We note that in our experiments, the sensitivity of electrodes containing a point defect density below n_{0D}^* , including those made of pristine graphene, was below the measurable limit of our readout system (the magenta dashed line in Figure 3b). From the data, we also found that upon transition into stage (ii), which includes the CF electrode, S_A no longer follows the linear trend. These results clearly illustrate the critical role of point defects in the sensitivity of graphene electrodes.

Uncovering the tight linear relationship between S_A and the point defect density in our preliminary sensing experiments has

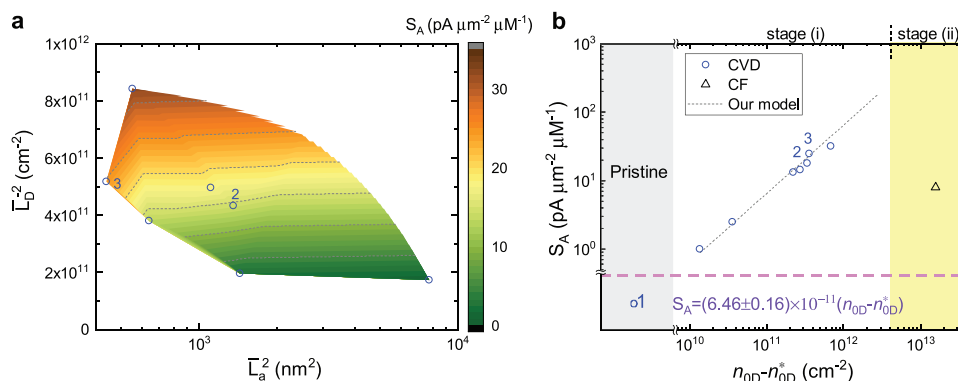


Figure 3. Revealing the link between structural defects and electrode sensitivity. a) Contour plot of S_A vs \bar{L}_a^2 and \bar{L}_D^{-2} , indicating that the sensitivity of the CVD sensors in stage (i) was largely independent of the average density of line defects and was amplified by increasing the average density of point defects. b) We found that S_A of the CVD sensors in stage (i) was amplified in linear proportion to the density of point defects, and dropped upon transition into stage (ii) (yellow shading). The magenta dashed line represents the measurable limit of S_A in our sensor readout system. The error bars of S_A were too small to show in the plot. The sensitivity of electrodes from pristine graphene was below the measurable limit. The numbers next to the data correspond to the sensors in Figure 2b.

two important consequences. The first one relates to the development of a sensor device technology. If this tight relationship is valid for the entire range of defects in stage (i), it suggests an opportunity for precise engineering of the sensitivity by controlling only the amounts of point defects using the empirical equation (Equation (1)). The second significance of our observation is fundamental to understanding the electron transfer in graphene. Specifically, the observed linear trend allowed us to propose and subsequently test a simplified microscopic model (discussed next) that can quantitatively and accurately explain the relationship between sensitivity and point defect density in graphene electrodes.

The linear relationship between S_A and n_{OD} in Figure 3b provides strong evidence that each point defect in stage (i) of the amorphization trajectory acts as an independent active electrochemical site. On the basis of this evidence, we propose a microscopic model to quantitatively explain the apparent linear relationship between the sensitivity and the density of point defects in graphene sensors. Our model builds on the assumption that the point defects in our multilayer graphene films are predominantly vacancies and the equilibrium concentration of topological point defects (e.g., Stone–Wales defects) is negligible.^[52,57] Given the high formation energy of Stone–Wales

defects (the simplest form of a topological point defect) in graphene,^[58] this is a reasonable assumption. Based on this assumption, we developed our microscopic model by utilizing three established phenomena related to the physics of the vacancy defects in graphene, discussed below.

The first phenomenon relates to the increase in the density of states (DOS) of multilayer graphene with the spatial density of point defects. Past theoretical studies predict that vacancy-type disorders in the graphene lattice with a sub-nanometer length scale behave similarly, in that they each locally alter the electronic band structure of graphene at the defect site by creating almost the same amounts of excess DOS at an energy corresponding to the Dirac point, E_D .^[59] Figure 4a schematically illustrates this phenomenon. These theoretical expectations are supported by past STM studies^[60,61] that demonstrated an increase of the local density of states (LDOS) at point defect sites. Moreover, those studies have shown that the electronic perturbations induced by the vacancy defects have a length scale of about 5 nm diameter.^[60,61] At this length scale, uniformly spaced point defects formed during stage (i) of the graphene amorphization trajectory (i.e., $L_D \geq 5$ nm) are spatially nonoverlapping (Figure 4b). Hence, we expect that DOS at E_D in this regime will increase in linear proportion to the spatial

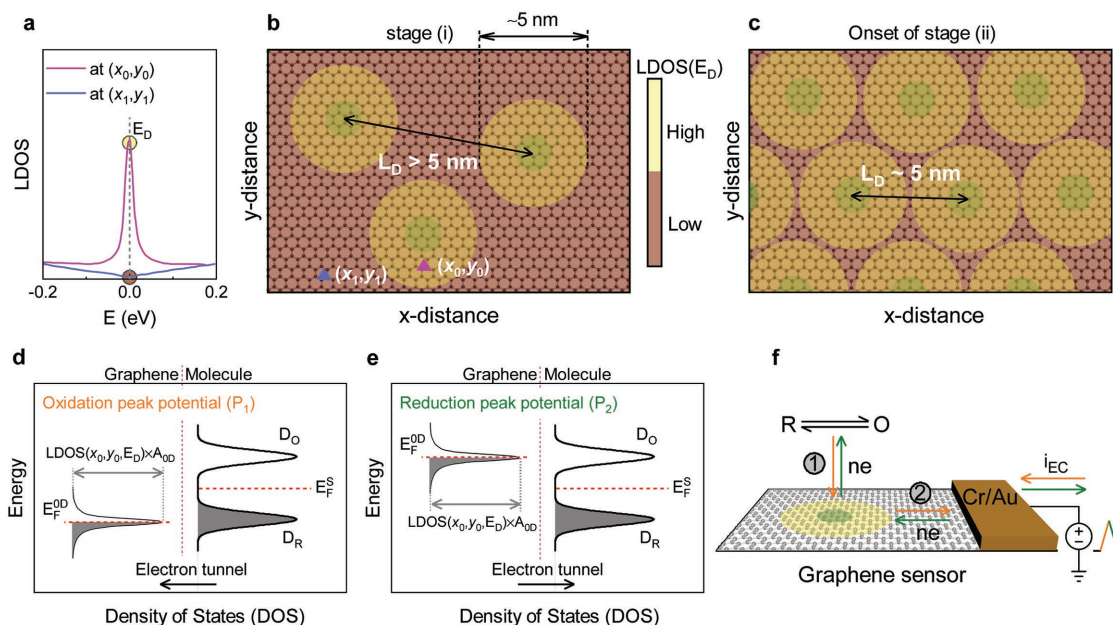


Figure 4. Proposed microscopic model of the electrode sensitivity. a) Schematic illustration of LDOS at a vacancy point defect site (x_0, y_0) and a defect-free region of graphene (x_1, y_1). These point defects induce localized electronic states at the Dirac point, E_D . b, c) Schematic illustrations of LDOS distribution at E_D across a graphene surface in stage (i) and the onset of stage (ii) of the amorphization trajectory, respectively. The green circles represent the structural disorder in graphene lattice with a sub-nanometer length scale. The yellow circles denote the excess electronic states induced by the point defects with a length scale of 5 nm diameter. d, e) Proposed local energy band diagram at each point defect site, corresponding to the oxidation peak potential P_1 and the reduction peak potential P_2 , respectively. These potentials are marked in Figure 1e. In sensing measurements, the FSCV voltage is applied to the graphene electrode and measured with respect to the potential of the solution. The solution potential is constant and serves as the voltage reference. E_F^{OD} and E_F^S denote the quasi-Fermi levels in the graphene and in the solution, respectively. Note that the E_F^{OD} follows the voltage due to the Fermi level pinning by the point defects. D_R and D_O are the DOS of the reductant (e.g., DA) and the oxidant (e.g., DOQ), respectively. The arrows in those plots indicate the direction of electron tunneling. Gray shading denotes filled energy states on both sides of the interface between the graphene and the molecule (magenta dashed line). f) Our model captures the underlying mechanisms of the FSCV sensitivity from nanoscale to macroscale. Localization of the defect-induced states in the out-of-plane direction at each point defect site facilitates the electron transfer (step 1). n denotes the number of electrons involved in this example redox reaction. Due to the delocalization of the defect-induced electronic states in the in-plane direction, the transferred electrons between the molecule and the defect become mobile charge carriers in graphene and are transported to the metal contact (step 2). The collective contribution of nanoscale defects produces a macroscopic redox current i_{EC} .

density of point defects, n_{0D} . Specifically, the electronic DOS of graphene (per unit area) at the Dirac point in stage (i) of the amorphization trajectory can be estimated from the following expression

$$\text{DOS}(E_D) = \sum_y \sum_x \text{LDOS}(x, y, E_D) \approx A_{0D} \times n_{0D} \times \text{LDOS}(x_0, y_0, E_D) \quad (2)$$

where A_{0D} and $\text{LDOS}(x_0, y_0, E_D)$, respectively, represent the average area of the electronic perturbation due to a single point defect (i.e., the area of the yellow circles in Figure 4b) and the local density of states at a point defect site at an energy of E_D . In the approximation on the right-hand side of the equation, we ignored the LDOS of the defect-free graphene regions at E_D . This is a reasonable assumption given the significantly smaller LDOS of those regions at E_D compared with the defect sites, as shown in Figure 4a.^[59,61] The linear increase of $\text{DOS}(E_D)$ with n_{0D} is expected to persist in stage (i) until the electronic states induced by the point defects begin to overlap (see Figure 4c), corresponding to the onset of the transition to stage (ii) of the amorphization trajectory.

The second phenomenon relates to the fact that the electronic state induced by a vacancy point defect in graphene, shown in Figure 4a, is pinned to the Fermi energy at the Dirac point E_D .^[61–65] Specifically, the pinning of the Fermi level occurs only in the regions of graphene, where the electronic band structure is modified by the vacancy defect (the yellow circles in Figure 4b). We denote the Fermi level in those regions of graphene as E_F^{0D} . In contrast, the Fermi level at the defect-free regions of graphene remains unpinned. An important consequence of the Fermi level pinning at the vacancy defect states is that those electronic states move with E_F^{0D} when a voltage bias is applied to graphene. As a result, during the sensing experiments, those defect-induced electronic states follow the FSCV voltage waveform applied to the graphene electrode. In Figure 4d and e, we schematically show the local energy band diagrams of the graphene–molecule system at a point defect site in a direction perpendicular to the graphene surface (i.e., out-of-plane direction). These two band diagrams, respectively, correspond to the FSCV voltages at which the peak oxidation and peak reduction occur. Specifically, when the defect-induced states align with the DOS of a molecule (either the reductant states D_R or oxidant states D_O), the electron transfer between the molecule and the point defect occurs. In these band diagrams, note the directions of the electron transfer (via tunneling) between the molecule and the point defect in graphene.

Finally, the Fermi energy states induced by the vacancy point defect sites in graphene are localized in the out-of-plane direction and delocalized in the in-plane direction.^[65] Localization in the out-of-plane direction facilitates electron transfer between the molecule and the point defects. On the other hand, delocalization in the in-plane direction allows lateral transport of the transferred electrons between each point defect site and the metal contact through the defect-free regions of graphene, as shown in Figure 4f. In particular, this property of the vacancy point defects allows the transferred electrons at different point defect sites to become mobile charge carriers in graphene, hence collectively produce a measurable redox current (i_{EC}).

The Gerischer–Marcus framework^[66,67] can be used to show that the electron transfer rate is approximately proportional

to the DOS of the electrode material at about the Fermi energy.^[68,69] This approximation together with the above-mentioned phenomena simplifies the quantification of the electron transfer rate. Specifically, because E_F^{0D} of graphene is pinned locally at each point defect site to E_D , and because $\text{DOS}(E_D)$ in the graphene electrode is linearly proportional to n_{0D} , the electron transfer rate and hence the area-normalized sensitivity of graphene scales in linear proportion with the average density of point defects in stage (i) of the amorphization trajectory. This proposed microscopic model supports our empirical equation for S_A obtained from the data in Figure 3b.

Our theoretical model, supported by the physics of vacancies in graphene, provides a powerful, quantitative framework for explaining the sensing mechanism in multilayer graphene electrodes based on the density of electronic states. Also, note that our proposed model of electron transfer for point defects is independent of the redox potential of the target molecule, and hence it can be applied to a variety of molecules as long as their redox potentials lie within the voltage range of FSCV.

On the basis of our observations in Figure 3 and the proposed microscopic model, we made the following hypotheses for engineering the FSCV sensitivity of electrochemical sensors made of multilayer graphene containing a variety of defect types. First, the synthesis process does not need to be optimized for line defects, because, as shown in Figure 3a, they had no observable effect on the electrode sensitivity of the CVD sensor samples. Second, the defect-free portion of the basal plane of graphene has no measurable contribution to the sensitivity. Third, the density of point defects alone is sufficient for accurately predicting the FSCV sensitivity of the electrode through the apparent linear relationship in stage (i), described by Equation (1). Fourth, the sensitivity degrades as the material structure transitions into stage (ii). Based on these hypotheses and the prediction of our microscopic model, we expect that the highest S_A can be obtained by maximizing the density of point defects in multilayer graphene before transitioning to stage (ii) of the amorphization trajectory. We tested these hypotheses using electrodes made of defect-engineered multilayer graphene, discussed next.

We directly tested the validity of our hypotheses in sensing experiments with electrodes fabricated from multilayer graphene with different amounts of point and line defects. Based on our microscopic model, we expect that these hypotheses can be generalized to different graphene production methods. Therefore, while Figure 3 was obtained from sensors produced using CVD, we tested the hypotheses on sensors produced by a different graphene production method. Further, we conducted the sensing experiments on two biologically active compounds, dopamine and serotonin.

We first developed a synthesis process that allowed us to engineer multilayer graphene films with different amounts of point and line defects. Of the various approaches for producing multilayer graphene,^[41,44,70–72] we adapted a method based on metal-induced transformation of amorphous carbon to multilayer graphene using a thin nickel catalyst.^[73,74] Our process involved creating amorphous carbon islands directly on SiO_2/Si substrates and graphitizing them at temperatures between 1000 and 1100 °C, as shown in Figure 5a (see Section S5 in the Supporting Information for details of the graphitization

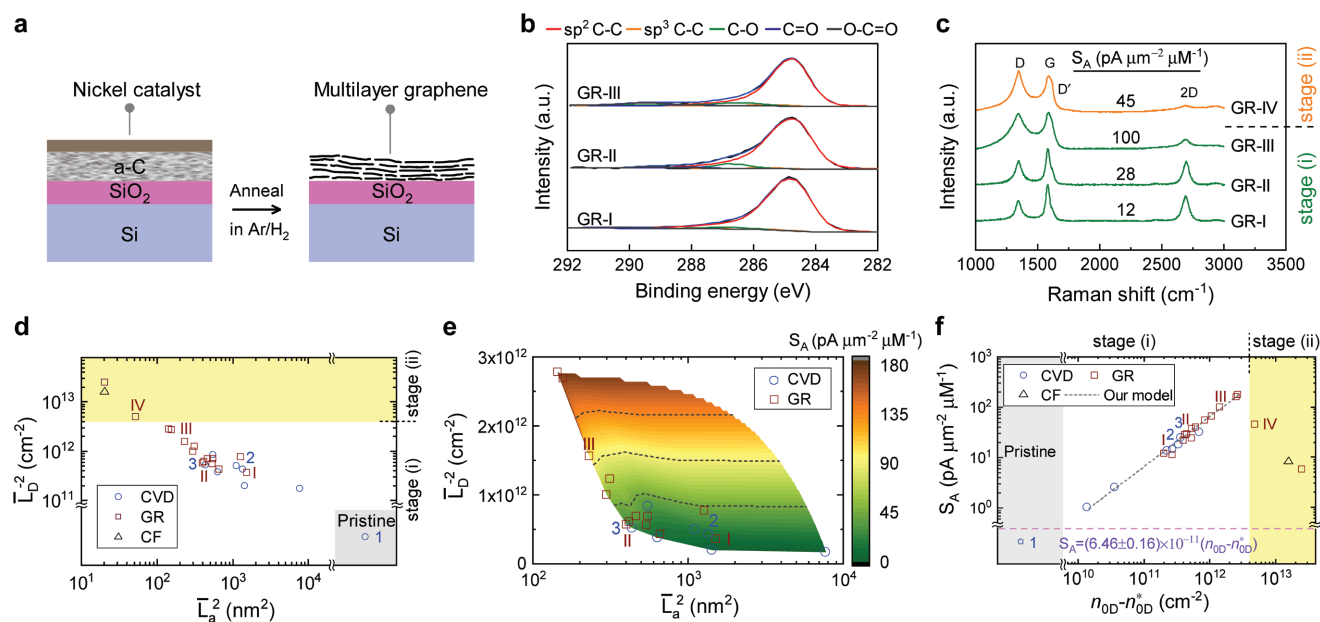


Figure 5. Engineered multilayer graphene sensors with predictable sensitivity. a) To test the validity of our hypotheses, supported by our microscopic model, we produced engineered multilayer graphene through nickel-induced graphitization of amorphous carbon (a-C). b) XPS measurements confirmed the graphitic nature of the films through the presence of sp^2 -hybridized C–C bond peak highlighted in red. c) We used Raman measurements to quantify the structural defects in our GR samples. d) We created three groups of GR samples: a first group that had overlapping density of point defects with the CVD sensors; a second group that contained a higher density of point defects than the CVD samples without transitioning to stage (ii); and a third group that had even higher density of point defects and was in stage (ii) (yellow shading). Numbers next to the data points denote the example GR (I, II, III, IV) and CVD (1, 2, 3) electrodes in (c) and Figure 1b, respectively. The error bars of \bar{L}_a^2 and \bar{L}_D^2 were too small to show in the plot. e) From the FSCV measurements of dopamine, we confirmed that the electrode sensitivity of the GR samples was largely independent of the crystallite size and increased with the point defect densities. f) We found that GR sensor samples with a similar density of point defects to CVD samples had the same S_A . By increasing the density of point defects in stage (i), we achieved a maximum S_A of about $177 \text{ pA } \mu\text{m}^{-2} \mu\text{M}^{-1}$, which is about 20 times higher than conventional CFs. The electrode sensitivity decreased rapidly once the structure of the carbon lattice transitioned into stage (ii). The magenta dashed line denotes the minimum measurable limit of S_A in our experiments. The error bars of S_A were too small to show in the plot.

process). We probed the graphitic structure of the samples using high-resolution X-ray photoelectron spectroscopy (XPS) (Figure 5b). Curve fitting of the XPS data indicated the sp^2 nature of the carbon–carbon bonds. The 2D peaks in Raman spectra of the films (Figure 5c) further confirmed the multilayer graphene growth. We observed that the structural properties of the multilayer graphene films made from this method are sensitive to the nickel thickness, annealing temperature, and growth time. By tuning these parameters, guided by Raman analysis, we could reliably and reproducibly generate samples with desired amounts of structural defects. We refer to these multilayer graphene samples as the *graphitized* samples.

In our experiments, we created three sets of GR sensor samples. The first group of sensor samples contained the same amounts of point defects as the CVD samples. This was to reproduce the sensitivity of those CVD electrodes and hence to demonstrate that our empirical equation of the electrode sensitivity is independent of the graphene production method. The second group of samples had significantly higher amounts of point defects than the CVD devices without transitioning to stage (ii). This set of GR samples allowed us to investigate the ability of our empirical equation for predicting S_A in the range of point defect densities that was not covered by the CVD sensor samples, hence testing the validity of our microscopic model. Further, using these samples we were able to explore the upper limit of S_A in stage (i). We also created a third group

of GR samples, which were in stage (ii) of the amorphization trajectory of graphene. These samples allowed us to confirm the drop in S_A upon transition into stage (ii). Figure 5c shows the representative Raman spectra of a few GR samples and their corresponding S_A for dopamine. In Figure 5d, we show the summary of average point and line defect densities for our engineered GR samples. In this plot, we have also included the CVD and CF samples to facilitate the distinction between the three groups of the GR samples. In addition to regions of overlap with the CVD and CF samples, note the region where the GR samples were engineered to have a significantly higher point defect density than the CVD samples without transitioning to stage (ii), the yellow shading in the plot.

We used miniaturized electrodes fabricated from defect-engineered GR films to perform FSCV measurements of dopamine (Figure S10, Supporting Information). Figure 5e shows the contour plot of S_A for the GR and CVD electrodes, where the multilayer graphene sensor electrodes are in stage (i). The plot shows that, like the CVD samples, the FSCV sensitivity of GR electrodes increased with the point defect density and was independent of the crystallite size. Plotting S_A as a function of the point defect density (see Figure 5f) revealed three critical results, confirming our hypotheses. First, the S_A of the GR sensors closely followed the same linear trend as the CVD samples, confirming that the average density of point defects was the main predictor of the S_A for multilayer

graphene films in stage (i). Specifically, the data points are well within the confidence bands of the linear regression (see Figure S20 in the Supporting Information), suggesting the statistical reproducibility of the electrode sensitivity for a particular defect density. Figures S22–S24 in the Supporting Information (Section S6) provide additional support for the reproducibility of the sensor manufacturing process. The exact method of production of the multilayer graphene film did not matter as long as the point defect density remained the same, hence confirming that our empirical equation of S_A can be generalized to other graphene production methods. Moreover, these results establish the validity of our microscopic model for quantitatively describing the FSCV sensitivity of graphene electrodes. Second, by increasing the density of point defects in stage (i), our model predicts that one could maximize S_A . Indeed, we achieved a remarkably high S_A of $177 \text{ pA } \mu\text{m}^{-2} \mu\text{M}^{-1}$ in response to dopamine, which is up to 20 times higher than the area-normalized FSCV sensitivities reported for CF electrodes in past studies.^[75,76] Third, our data indicate that S_A began to degrade at a point defect density corresponding to a L_D of about 5–6 nm, which coincides with the onset of graphene transition to stage (ii). Most strikingly, this length scale agrees with our proposed microscopic model in Figure 4, where the electronic perturbations at the point defects begin to overlap (Figure 4c). Conventional CF electrodes that are used for studying neurochemical changes in the brain^[36,38,75,77] are usually in this regime. Our finding explains the fundamentally small sensitivity of these electrodes and suggests a practical method to significantly boost the electrode sensitivity for such measurements.

To ensure that our results were not limited to a particular molecule, we also performed in vitro FSCV measurement of serotonin neurotransmitters using the multilayer graphene electrodes in stage (i). The results confirmed that the linear increase of electrode sensitivity with increasing average point defect density generalized to serotonin and was, therefore, a property of the electrode and not the measured analyte (Figures S25 and S26, Supporting Information).

To examine the role of oxygen functional groups in FSCV sensitivity of graphene electrodes to dopamine and serotonin, we performed XPS measurements on multiple multilayer graphene sensor electrodes with markedly different S_A . The electrodes were chosen from both CVD and GR sensor samples and the XPS measurements were performed immediately after the FSCV experiments in an ultrahigh-vacuum environment. By analyzing the XPS data (Figure S27, Supporting Information), we observed a noticeable variation in the amount of oxygen-containing groups among the sensors. This observation together with our finding that 99% of the variation in sensitivity is explained by the average density of point defects (R^2 of the linear regression in Figure 5f) suggests that the amount of oxygen functional groups is not a dominant factor in defining the sensitivity of multilayer graphene electrodes in FSCV measurements of dopamine and serotonin.

Our findings establish the fundamental principles for predicting the FSCV sensitivity of multilayer graphene electrochemical sensors to neurochemical molecules based on structural defects. Using these principles, we devised an approach for nanoengineering graphene, resulting in the reproducible and reliable fabrication of homogeneous sensors

with optimized sensitivity. We found that in a graphene sensor consisting of a variety of defects, the density of point defects can be used as the main predictor of the sensitivity. This is evident from the excellent agreement between the predictions of our empirical equation of the electrode sensitivity and the measured data (see Figure S21 in the Supporting Information). Moreover, the remarkably high sensitivity of our miniaturized electrodes is due to the maximization of point defect density while keeping the electrode material in stage (i) of the amorphization trajectory of graphene.

The density of line defects and oxygen-containing functional groups appear to have minimal bearing on the FSCV sensitivity of multilayer graphene electrodes to dopamine and serotonin. This observation simplifies the electrode manufacturing process by removing the need for monitoring and optimization of line defects and oxygen-containing groups. However, these functional groups may still be electrochemically active. Additional studies are required to explore the exact role of oxygen-containing groups and their interactions with point defects. An exciting possibility is to further increase the sensitivity of our nanoengineered electrodes by adding functional groups that amplify the effect of point defects.

The increase of electron transfer in graphene and other related materials due to the emergence of excess DOS in the electronic band structure is well known.^[26,27,78–80] However, less understood is how to reliably quantify the macroscopic electrode sensitivity in FSCV measurements using DOS of graphene. Our proposed model, supported by the physics of point defects, is the first to provide a theoretical framework that can allow the calculation of S_A in a graphene sensor containing point defects. Specifically, our model offers a quantitative and accurate understanding of the underlying mechanisms that shape the FSCV sensitivity of graphene electrodes, from the electron transfer at the defect sites to the collection of those charge carriers by the metal contact made to the graphene electrode.

Uncovering the linear relationship between S_A and the density of point defects through FSCV of neurochemical molecules was critical for developing the microscopic model of the electrode sensitivity. We were able to uncover this linear relationship because of the accuracy and reproducibility of our material characterization, device fabrication process, and sensing measurements. In particular, we attribute the reliability of our sensing measurements primarily to our use of multilayer graphene as the electrode material, hence mitigating the interference from the charge impurities at the graphene–SiO₂ interface. This is consistent with the findings of a previous SECCM study, demonstrating that whereas multilayer graphene is immune to substrate effects, using SiO₂ substrate causes noticeable fluctuations in electron transfer of monolayer graphene.^[27]

The underlying mechanisms of electron transfer in our model are independent of the number of layers in graphene. Therefore, though we used multilayer graphene in these experiments, we expect our findings to hold for sensors made of graphene with different number of layers, i.e., monolayer, bilayer, or more. In the case of monolayer graphene, however, given that its inherent electron transfer is very susceptible to stray charges in the substrate,^[27] care must be taken when using monolayer graphene sensors for conducting similar experiments.

Note that in our experiments, we have examined the FSCV response of the graphene sensors for dopamine and serotonin molecules. An exciting future direction is to investigate whether the findings of our paper extend to other redox reactions including those of outer sphere systems. Those future studies include testing the validity of the linear relationship between the FSCV sensitivity and the average density of point defects in stage (i) for other redox systems, and hence confirming the generalizability of the microscopic model.

In this study, we used Raman spectroscopy to classify the structural disorders in our multilayer graphene films based on their dimensionality. We next defined the subtypes of these defects in our multilayer graphene films. In the case of point defects, Raman is unable to distinguish between topological (e.g., Stone–Wales) and vacancy point defects, since both of these subtypes of point defects are symmetry breaking and hence influence the Raman D band. However, for two reasons, we can infer that the point defects present in our material are predominantly vacancies. First, topological point defects have high formation energy; hence, they rarely form naturally except in extreme conditions (e.g., rapid quenching from high temperatures or under irradiation).^[52,57] However, topological defects in graphene are more likely to appear in the form of line defects such as dislocations and grain boundaries.^[81] Second, our proposed microscopic model is based on the physics of vacancy point defects in graphene. Since our model is able to accurately explain the experimental data, we speculate that the vacancy point defects are the dominant factor in shaping the electrode sensitivity.

The AFM studies of the surface morphology showed that our graphene electrodes mostly consist of basal planes with minimal density of step edges. Thus, we suggest that the line defects in our multilayer graphene films are predominantly dislocations and grain boundaries. Additional studies that explore the relationship between specific subtypes of defects and the electrode sensitivity (e.g., using STM) will be useful in further refining the theory of the sensor operation.

Our proposed quantitative paradigm has far-reaching practical implications. By providing guidelines for optimizing the FSCV sensitivity of carbon-based electrochemical sensors to neuromodulators such as dopamine and serotonin, we enable significant improvements in a wide range of applications from a next generation of neural probes to multiplexed lab-on-a-chip sensing platforms. Specifically, our precise nanoengineering methodology can ensure fabrication of sensor arrays with predictable and homogeneous sensitivity (see Figure S22 in the Supporting Information). This represents an important first step toward the implementation of nanoengineered carbon-based electrodes suitable for compact, multichannel sensor systems required in large-scale applications. Further, our nanoengineered electrodes overcome an existing obstacle for industrial-scale fabrication of reliable sensors with reproducible electrode sensitivity. Current methods for fabrication of carbon-based electrodes are not developed to optimize the density of point defects. Consequently, they are largely dependent on post-manufacturing measurement for calibration of sensors and are prone to producing minimally responsive sensors that have to be discarded. In contrast, our paradigm enables industrial-scale and targeted nanomanufacturing of carbon-based electrodes that have sensitivity levels far beyond their predecessors.

Experimental Section

Multilayer Graphene Films: CVD multilayer graphene samples were obtained from two commercial vendors: Graphene Supermarket and Graphene Platform, Inc. The CVD films were grown on nickel foils, which were then removed chemically during the layer-transfer process using the commercial nickel etchant TFG (Transene Company Inc.). The freestanding CVD films were subsequently mounted on p⁺ silicon substrates capped with 285 nm thermally grown SiO₂. The graphitized samples were produced using a custom-made system. Details of the metal-induced graphitization process are given in Section S5 of the Supporting Information.

Raman Measurements: To quantify the structural defects in multilayer graphene films, Raman measurements were performed using Horiba Xplora μ-Raman system with a 532 nm incident laser. The Raman spectra were fitted using Lorentzian and Gaussian functions, providing the full width at half maximum and area of the G and D peaks. The curve fitting results were then used to extract the density of line and point defects according to the theoretical simulations described in ref. [35]. Details of the Raman analysis are given in Section S4 of the Supporting Information.

FSCV Measurements: To examine the electrode sensitivity, FSCV measurements of dopamine and serotonin (Sigma-Aldrich) were performed using a triangular voltage waveform with a scan rate of 400 V s⁻¹ and a repetition frequency of 10 Hz. The FSCV current signal was measured using a low-noise current amplifier (SR570, Stanford Research Systems) and subsequently digitized using a data acquisition card (NI 6353 X series, National Instruments). A MATLAB control interface was used to operate these instruments. For sensing measurements, the biomolecules were dissolved in a 1× phosphate-buffered saline (PBS) solution. PBS was prepared using the recipe in ref. [82].

Supporting Information

Supporting Information is available from the Wiley Online Library or from the author.

Acknowledgements

T.W. and A.A. contributed equally to this work. This research used resources of the Center for Functional Nanomaterials, which is a U.S. DOE Office of Science Facility, at Brookhaven National Laboratory under Contract No. DE-SC0012704. The authors also acknowledge the Surface Science Facility of CUNY Advanced Science Research Center for the use of the XPS tool. D.S. acknowledges partial financial support by NSF-CMMI award 1728051. R.K. was supported by the National Institute of Mental Health grant R01MH109180, a Pew Scholarship in the Biomedical Sciences, and Simons Collaboration on the Global Brain. The authors acknowledge J. Uichanco for helpful discussions. T.W., A.A., D.S., and R.K. designed research; T.W., A.A., and D.S. performed research; T.W., A.A., D.S., and R.K. analyzed data; and T.W., A.A., D.S., and R.K. wrote the paper.

Conflict of Interest

The authors acknowledge the following patent applications: U.S. Serial No. 62/599303 and U.S. Serial No. 62/539045.

Keywords

density of states, electrochemical sensors, electron transfer, fast-scan cyclic voltammetry, graphene, sensitivity, structural defects

Received: September 4, 2018

Revised: November 11, 2018

Published online:

- [1] W. Gao, S. Emaminejad, H. Y. Y. Nyein, S. Challa, K. Chen, A. Peck, H. M. Fahad, H. Ota, H. Shiraki, D. Kiriya, D.-H. Lien, G. A. Brooks, R. W. Davis, A. Javey, *Nature* **2016**, *529*, 509.
- [2] X. Xuan, M. F. Hossain, J. Y. Park, *Sci. Rep.* **2016**, *6*, 33125.
- [3] B. Nasri, T. Wu, A. Alharbi, K. You, M. Gupta, S. P. Sebastian, R. Kiani, D. Shahrjerdi, *IEEE Trans. Biomed. Circuits Syst.* **2017**, *11*, 1192.
- [4] X. Xuan, H. S. Yoon, J. Y. Park, *Biosens. Bioelectron.* **2018**, *109*, 75.
- [5] Y. Shao, J. Wang, H. Wu, J. Liu, I. A. Aksay, Y. Lin, *Electroanalysis* **2010**, *22*, 1027.
- [6] C. B. Jacobs, M. J. Peairs, B. J. Venton, *Anal. Chim. Acta* **2010**, *662*, 105.
- [7] Z. Zhu, *Nano-Micro Lett.* **2017**, *9*, 25.
- [8] E. Sinkala, J. E. McCutcheon, M. J. Schuck, E. Schmidt, M. F. Roitman, D. T. Eddington, *Lab Chip* **2012**, *12*, 2403.
- [9] R. J. Rice, N. M. Pontikos, R. L. McCreery, *J. Am. Chem. Soc.* **1990**, *112*, 4617.
- [10] R. L. McCreery, *Chem. Rev.* **2008**, *108*, 2646.
- [11] C. E. Banks, T. J. Davies, G. G. Wildgoose, R. G. Compton, *Chem. Commun.* **2005**, 829.
- [12] C. E. Banks, R. G. Compton, *Analyst* **2006**, *131*, 15.
- [13] X. Ji, C. E. Banks, W. Xi, S. J. Wilkins, R. G. Compton, *J. Phys. Chem. B* **2006**, *110*, 22306.
- [14] D. A. Brownson, C. E. Banks, *The Handbook of Graphene Electrochemistry*, Springer, London, UK **2014**.
- [15] A. C. Schmidt, X. Wang, Y. Zhu, L. A. Sombers, *ACS Nano* **2013**, *7*, 7864.
- [16] G. P. Keeley, N. McEvoy, H. Nolan, M. Holzinger, S. Cosnier, G. S. Duesberg, *Chem. Mater.* **2014**, *26*, 1807.
- [17] G. Gao, M. Pan, C. D. Vecitis, *J. Mater. Chem. A* **2015**, *3*, 7575.
- [18] C. Chung, Y. K. Kim, D. Shin, S. R. Ryoo, B. H. Hong, D. H. Min, *Acc. Chem. Res.* **2013**, *46*, 2211.
- [19] S. C. S. Lai, A. N. Patel, K. McKelvey, P. R. Unwin, *Angew. Chem., Int. Ed.* **2012**, *51*, 5405.
- [20] A. N. Patel, M. G. Collignon, M. A. O'Connell, W. O. Y. Hung, K. McKelvey, J. V. Macpherson, P. R. Unwin, *J. Am. Chem. Soc.* **2012**, *134*, 20117.
- [21] A. N. Patel, K. McKelvey, P. R. Unwin, *J. Am. Chem. Soc.* **2012**, *134*, 20246.
- [22] A. N. Patel, S.-Y. Tan, P. R. Unwin, *Chem. Commun.* **2013**, *49*, 8776.
- [23] G. Zhang, A. S. Cuharuc, A. G. Güell, P. R. Unwin, *Phys. Chem. Chem. Phys.* **2015**, *17*, 11827.
- [24] P. L. Frederix, P. D. Bosshart, T. Akiyama, M. Chami, M. R. Gullo, J. J. Blackstock, K. Dooleweerd, N. F. De Rooij, U. Staufer, A. Engel, *Nanotechnology* **2008**, *19*, 384004.
- [25] A. Anne, M. A. Bahri, A. Chovin, C. Demaille, C. Taoufenua, *Phys. Chem. Chem. Phys.* **2014**, *16*, 4642.
- [26] J. H. Zhong, J. Zhang, X. Jin, J. Y. Liu, Q. Li, M. H. Li, W. Cai, D. Y. Wu, D. Zhan, B. Ren, *J. Am. Chem. Soc.* **2014**, *136*, 16609.
- [27] A. G. Güell, A. S. Cuharuc, Y. R. Kim, G. Zhang, S. Y. Tan, N. Ebejer, P. R. Unwin, *ACS Nano* **2015**, *9*, 3558.
- [28] R. McCreery, A. Bergren, A. Morteza-Najarian, S. Y. Sayed, H. Yan, *Faraday Discuss.* **2014**, *172*, 9.
- [29] S. P. E, Y. R. Kim, D. P. Perry, C. L. Bentley, P. R. Unwin, *ACS Appl. Mater. Interfaces* **2016**, *8*, 30458.
- [30] L. Jiang, W. Fu, Y. Y. Birdja, M. T. M. Koper, G. F. Schneider, *Nat. Commun.* **2018**, *9*, 793.
- [31] F. Tuinstra, J. L. Koenig, *J. Chem. Phys.* **1970**, *53*, 1126.
- [32] L. G. Cançado, K. Takai, T. Enoki, M. Endo, Y. A. Kim, H. Mizusaki, A. Jorio, L. N. Coelho, R. Magalhães-Paniago, M. A. Pimenta, *Appl. Phys. Lett.* **2006**, *88*, 163106.
- [33] M. M. Lucchese, F. Stavale, E. H. M. Ferreira, C. Vilani, M. V. O. Moutinho, R. B. Capaz, C. A. Achete, A. Jorio, *Carbon* **2010**, *48*, 1592.
- [34] L. G. Cançado, A. Jorio, E. H. M. Ferreira, F. Stavale, C. A. Achete, R. B. Capaz, M. V. O. Moutinho, A. Lombardo, T. S. Kulmala, A. C. Ferrari, *Nano Lett.* **2011**, *11*, 3190.
- [35] L. G. Cançado, M. G. D. Silva, E. H. M. Ferreira, F. Hof, K. Kampioti, K. Huang, A. Pénicaud, C. A. Achete, R. B. Capaz, A. Jorio, *2D Mater.* **2017**, *4*, 025039.
- [36] R. M. Wightman, L. J. May, A. C. Michael, *Anal. Chem.* **1988**, *60*, 769A.
- [37] R. M. Wightman, D. L. Robinson, *J. Neurochem.* **2002**, *82*, 721.
- [38] K. T. Kishida, I. Saez, T. Lohrenz, M. R. Witcher, A. W. Laxton, S. B. Tatter, J. P. White, T. L. Ellis, P. E. M. Phillips, P. R. Montague, *Proc. Natl. Acad. Sci. USA* **2016**, *113*, 200.
- [39] W. G. Kuhr, R. M. Wightman, *Brain Res.* **1986**, *381*, 168.
- [40] B. J. Venton, R. M. Wightman, *Anal. Chem.* **2003**, *75*, 414 A.
- [41] A. Reina, X. Jia, J. Ho, D. Nezich, H. Son, V. Bulovic, M. S. Dresselhaus, J. Kong, *Nano Lett.* **2009**, *9*, 30.
- [42] X. Li, C. W. Magnuson, A. Venugopal, R. M. Tromp, J. B. Hannon, E. M. Vogel, L. Colombo, R. S. Ruoff, *J. Am. Chem. Soc.* **2011**, *133*, 2816.
- [43] X. Li, Y. Zhu, W. Cai, M. Borysiak, B. Han, D. Chen, R. D. Piner, L. Colombo, R. S. Ruoff, *Nano Lett.* **2009**, *9*, 4359.
- [44] K. S. Kim, Y. Zhao, H. Jang, S. Y. Lee, J. M. Kim, K. S. Kim, J. H. Ahn, P. Kim, J. Y. Choi, B. H. Hong, *Nature* **2009**, *457*, 706.
- [45] Y. Lee, S. Bae, H. Jang, S. Jang, S.-E. Zhu, S. H. Sim, Y. I. Song, B. H. Hong, J.-H. Ahn, *Nano Lett.* **2010**, *10*, 490.
- [46] E. S. Bucher, R. M. Wightman, *Annu. Rev. Anal. Chem.* **2015**, *8*, 239.
- [47] P. W. Glimcher, *Proc. Natl. Acad. Sci. USA* **2011**, *108*, 15647.
- [48] S. B. Floresco, *Annu. Rev. Psychol.* **2015**, *66*, 25.
- [49] R. M. Costa, *Curr. Opin. Neurobiol.* **2011**, *21*, 579.
- [50] G.-D. Lee, C. Z. Wang, E. Yoon, N.-M. Hwang, D.-Y. Kim, K. M. Ho, *Phys. Rev. Lett.* **2005**, *95*, 205501.
- [51] L. Vicarelli, S. J. Heerema, C. Dekker, H. W. Zandbergen, *ACS Nano* **2015**, *9*, 3428.
- [52] F. Banhart, J. Kotakoski, A. V. Krasheninnikov, *ACS Nano* **2011**, *5*, 26.
- [53] L. L. Zhang, X. Zhao, H. Ji, M. D. Stoller, L. Lai, S. Murali, S. McDonnell, B. Cleveger, R. M. Wallace, R. S. Ruoff, *Energy Environ. Sci.* **2012**, *5*, 9618.
- [54] A. C. Ferrari, *Solid State Commun.* **2007**, *143*, 47.
- [55] A. C. Ferrari, D. M. Basko, *Nat. Nanotechnol.* **2013**, *8*, 235.
- [56] R. Beams, L. G. Cançado, L. Novotny, *Nano Lett.* **2011**, *11*, 1177.
- [57] J. Kotakoski, J. C. Meyer, S. Kurasch, D. Santos-Cottin, U. Kaiser, A. V. Krasheninnikov, *Phys. Rev. B* **2011**, *83*, 245420.
- [58] L. Li, S. Reich, J. Robertson, *Phys. Rev. B* **2005**, *72*, 184109.
- [59] J. Mao, Y. Jiang, D. Moldovan, G. Li, K. Watanabe, T. Taniguchi, M. R. Masir, F. M. Peeters, E. Y. Andrei, *Nat. Phys.* **2016**, *12*, 545.
- [60] P. Ruffieux, M. Melle-Franco, O. Gröning, M. Biemann, F. Zerbetto, P. Gröning, *Phys. Rev. B* **2005**, *71*, 153403.
- [61] M. M. Ugeda, I. Brihuega, F. Guinea, J. M. Gómez-Rodríguez, *Phys. Rev. Lett.* **2010**, *104*, 096804.
- [62] S. Massabeau, M. Baillergeau, T. Phuphachong, C. Berger, W. A. de Heer, S. Dhillon, J. Tignon, L. A. de Vaulchier, R. Ferreira, J. Mangeney, *Phys. Rev. B* **2017**, *95*, 085311.
- [63] V. M. Pereira, F. Guinea, J. M. B. Lopes dos Santos, N. M. R. Peres, A. H. Castro Neto, *Phys. Rev. Lett.* **2006**, *96*, 036801.
- [64] V. M. Pereira, J. M. B. Lopes dos Santos, A. H. Castro Neto, *Phys. Rev. B* **2008**, *77*, 115109.
- [65] A. M. Valencia, M. J. Caldas, *Phys. Rev. B* **2017**, *96*, 125431.
- [66] H. Gerischer, *Physical Chemistry: An Advanced Treatise*, Vol. 9A, Academic Press, Inc., New York **1970**.
- [67] R. A. Marcus, *Pure Appl. Chem.* **1997**, *69*, 13.
- [68] A. J. Bard, L. R. Faulkner, J. Leddy, C. G. Zoski, *Electrochemical Methods: Fundamentals and Applications*, Vol. 2, Wiley, New York **1980**.
- [69] N. Sato, *Electrochemistry at Metal and Semiconductor Electrodes*, Elsevier Science, Amsterdam, The Netherlands **1998**.

- [70] K. Wang, G. Tai, K. H. Wong, S. P. Lau, W. Guo, *AIP Adv.* **2011**, *1*, 022141.
- [71] J. Hass, W. A. d. Heer, E. H. Conrad, *J. Phys.: Condens. Matter* **2008**, *20*, 323202.
- [72] H. Cao, Q. Yu, R. Colby, D. Pandey, C. S. Park, J. Lian, D. Zemlyanov, I. Childres, V. Drachev, E. A. Stach, M. Hussain, H. Li, S. S. Pei, Y. P. Chen, *J. Appl. Phys.* **2010**, *107*, 044310.
- [73] J. A. Rodríguez-Manzo, C. Pham-Huu, F. Banhart, *ACS Nano* **2011**, *5*, 1529.
- [74] D. Berman, S. A. Deshmukh, B. Narayanan, S. K. R. S. Sankaranarayanan, Z. Yan, A. A. Balandin, A. Zinovev, D. Rosenmann, A. V. Sumant, *Nat. Commun.* **2016**, *7*, 12099.
- [75] E. W. Schluter, A. R. Mitz, J. F. Cheer, B. B. Averbeck, *PLoS One* **2014**, *9*, e98692.
- [76] M. K. Zachek, P. Takmakov, B. Moody, R. M. Wightman, G. S. McCarty, *Anal. Chem.* **2009**, *81*, 6258.
- [77] D. L. Robinson, B. J. Venton, M. L. A. V. Heien, R. M. Wightman, *Clin. Chem.* **2003**, *49*, 1763.
- [78] K. K. Cline, M. T. McDermott, R. L. McCreery, *J. Phys. Chem.* **1994**, *98*, 5314.
- [79] G. Winterer, D. R. Weinberger, *Trends Neurosci.* **2004**, *27*, 683.
- [80] R. L. McCreery, M. T. McDermott, *Anal. Chem.* **2012**, *84*, 2602.
- [81] O. V. Yazyev, S. G. Louie, *Phys. Rev. B* **2010**, *81*, 195420.
- [82] B. Chazotte, *Cold Spring Harb. Protoc.* **2012**, 913, <https://doi.org/10.1101/pdb.prot5571>.